A method for constrained optimisation of the design of a scanning helium microscope

M. Bergin*, D.J. Ward, J. Ellis, A.P. Jardine

Cavendish Laboratory, JJ Thomson Avenue, Cambridge, UK

Abstract

We describe a method for obtaining the optimal design of a normal incidence Scanning Helium Microscope (SHeM). Scanning helium microscopy is a recently developed technique that uses low energy neutral helium atoms as a probe to image the surface of a sample without causing damage. After estimating the variation of source brightness with nozzle size and pressure, we perform a constrained optimisation to determine the optimal geometry of the instrument (i.e. the geometry that maximises intensity) for a given target resolution. For an instrument using a pinhole to form the helium microprobe, the source and atom optics are separable and Lagrange multipliers are used to obtain an analytic expression for the optimal parameters. For an instrument using a zone plate as the focal element, the whole optical system must be considered and a numerical approach has been applied. Unlike previous numerical methods for optimisation, our approach provides insight into the effect and significance of each instrumental parameter, enabling an intuitive understanding of effect of the SHeM geometry. We show that for an instrument with a working distance of 1 mm, a zone plate with a minimum feature size of 25 nm becomes the advantageous focussing element if the desired beam standard deviation is below about 300 nm.

Keywords: Scanning helium microscopy, Atomic microscopy, Neutral atom microscope, Fresnel zone plate, Constrained optimisation

1. Introduction

Scanning helium microscopy (SHeM) is a form of microscopy which uses low energy (5-100 meV) helium atoms to image the surface of a material or structure. Helium atoms have long been used as a probe for surfaces in reciprocal space due to their low energy and inertness. The concept of a spatially resolved helium scattering instrument was originally demonstrated in transmission by Koch et al. [1], using a Fresnel zone plate to focus the atoms. The method was later extended to reflection mode by Witham and Sanchez [2], who used a pinhole to collimate the beam. The pinhole geometry has also been utilised in instruments developed by collaborating researchers in Cambridge, UK and Newcastle, Australia [3, 4]. In the established technique of electron microscopy, the high energy beams needed to image fine details can lead to significant amounts of damage [5]. Similarly, with the exception of the environmental scanning electron microscopy [6], charging generally limits the technique to conductive, or conductively coated, surfaces. In contrast, since SHeM uses inert and neutral helium atoms, it can be used to study any delicate and insulating surfaces without any risk of damage or charging.

Figure 1 shows a schematic view of the main atom-optical elements in a normal incidence scanning helium microscope. The beam of atoms is formed through the supersonic expansion of helium into vacuum. The beam is collimated initially by a skimmer (typically 0.1-0.5 mm), then collimated or focussed by the 'main' optical element, which here we consider to be either a pinhole or zone-plate. The sample is then rastered in front of the helium microprobe, and atoms scattered in a particular direction are transferred to a detector, which is usually a high-sensitivity mass-spectrometer.

In all current implementations of helium microscopy the available signal level is a major limitation, due to the nature of the source and difficulty in ionisation and detection of helium atoms. The inertness and neutrality of the helium atoms that make it a good probe for imaging also lead to the atoms being difficult to manipulate and detect. Limited signal affects the signal to noise in images and, since the signal varies strongly with microprobe size, the ultimate usable resolution. Determining an optimised microscope geometry, which maximises signal levels while keeping the beam size to a minimum, is required to produce a design for a realistic helium microscope with an improved resolution.

Previous attempts to optimise the design of a SHeM typically treat the source and atom optics as separate problems that need solving. Palau et al. [7, 8] use Sikora's model [9, 10] for the centerline intensity downstream from the source. Optimal parameters for a zone plate and pinhole microscope are found by computing the intensity for a set of atom optics variables and finding the maximum. The use of the complex Sikora model (that can be avoided in the limit of small skimmers) and a substitution method for performing the optimisation means that the resulting algebra is lengthy, that few analytic expressions can be obtained and that in general the method can only be applied to experimental data if the data can be re-parameterised into a simple expression [11, 12]. Alternatively, Kaltenbacher has used

*Corresponding author
Email address: mb802@cam.ac.uk (M. Bergin)

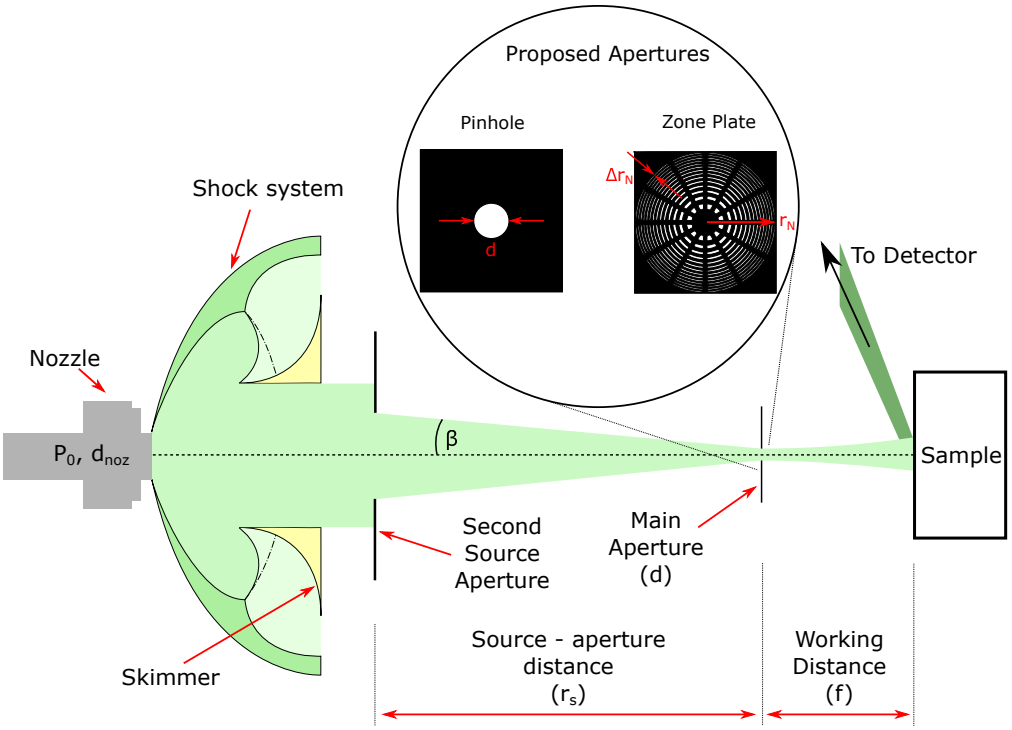

Figure 1: Schematic of a normal incidence scanning helium microscope. The beam is formed in a free jet nozzle expansion (left) and is initially collimated by a skimmer (centre-left). The shock structure is discussed in more detail in fig. 2. The beam is further collimated by an (optional) second aperture, in conjunction with suitable differential pumping. The beam passes into the sample region through either a pinhole or a zone plate (centre-right) and scatters from the sample (right). Atoms scattered into a particular solid-angle are collected and counted.

a multi-objective optimisation approach to design a complex atom optics setup involving two zone plates and a pinhole [13]. Kaltenbacher has used large approximations for the intensity and size of the beam, and using a multi-objective optimisation leads to Pareto-optimal solutions rather than direct solutions for a specific resolution. While both have provided useful solutions for particular cases, they are difficult to use to provide physical insight into a more general optimal microscope configuration.

A combined optimisation of both the source and atom optics is essential when considering a zone plate, due to the velocity spread of the beam affecting both the source brightness and the chromatic aberrations. We will show that increasing the brightness of the source and decreasing the helium beam size when using a zone plate are directly opposing objectives. Therefore, while it is possible to separate the problems when considering a pinhole, the only way to find an optimal design when using a zone plate with severe chromatic aberrations, is to use a model that includes both the source and atom optics.

In this paper, we outline a method to perform a simultaneous constrained optimisation of both the source and the atom optics, for a particular target resolution. After assuming a model for the intensity obtained from the source, the method produces a set of design criteria for future instruments aiming to achieve a particular resolution. Section 2 introduces the key theory needed to develop a model for the beam size and flux, in a machine with a normal incidence beam formed using either a pinhole or zone plate. Section 3 explains the analytic and numerical constrained optimisation procedure that is used. Section 4 presents key results from applying the constrained optimisation to the models we have for the beam. Section 5 provides a summary and conclusions that can be used as design criteria for future instruments.

2. Principal Components of model

2.1. Free jet expansion

The supersonic helium beam is formed in a free-jet gas expansion where high pressure gas (typically around 100 bar) expands through a fine nozzle (typically 10 µm) into a low pressure vacuum chamber [10]. The expansion is schematically represented in Fig. 2. The gas is accelerated by the pressure difference, reaching sonic speeds at the nozzle exit. The gas expands as it enters the chamber, but since the flow is supersonic the gas overexpands and a shock system is formed to recompress the system to match the chamber pressure. The resulting shock structure leaves a zone of silence where the expansion can be sampled, using the skimmer, to produce a high intensity beam with a narrow velocity distribution.

As evident from Fig. 1, a narrow helium microprobe generally requires a small angular source size, β, and future high resolution instruments will need to achieve a narrow beam without disrupting the expansion. The angular source size can be reduced either by moving the source further away from the main aperture, or by increasing the collimation of the helium expansion. Moving the source is the simplest method, but increases the overall size of the instrument to an impractical degree. Very

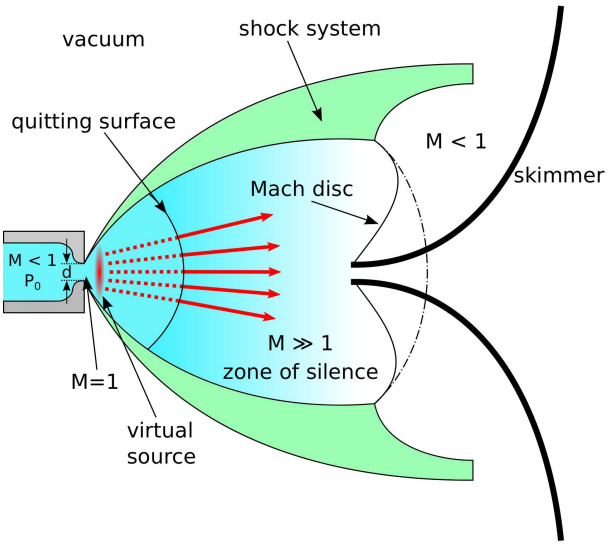

Figure 2: Schematic representation of a free jet expansion. Gas exits the nozzle at supersonic speeds and begins to expand adiabatically in the vacuum. Shock structures caused by the over expanding gas meeting the vacuum boundary conditions create the barrel shocks and a Mach disk. A conical skimmer is placed before the Mach disk, to extract a beam of atoms. The imaginary boundary where the flow transitions to free molecular flow is shown as the 'quitting surface'. Trajectories of atoms after the quitting surface are shown in red and can be traced back to a 'virtual source' where the atoms appear to have originated. Based on fig. 2.1 by Scoles. [10] and fig. 1 by Barr et al. [14]

small skimmers (often known as 'microskimmers' [15]) can be used to reduce the source size, but their narrow geometry means atoms backscattered into the beam from either the leading edge, or the internal skimmer walls, risks affecting the beam intensity significantly. An alternative is to introduce a second aperture behind the skimmer that, provided the volume is adequately pumped, will set the source size of the instrument whilst minimising additional beam interference [16].

The parallel velocity distribution of the atom beam is often described by a speed ratio, S, which is the mean velocity of the beam divided by the thermal spread in velocities [10]. The speed ratio can be approximately related to the wavelength distribution of the beam through $S = \overline{\lambda}/(\sqrt{2}\Delta\lambda)$, where $\overline{\lambda}$ is the average wavelength of the beam and $\Delta\lambda$ is the standard deviation of the wavelength distribution [17].

Quantum effects cause beams of helium-4 atoms formed in a free jet expansion to have an unusually high speed ratio; a property which is exploited in many surface scattering experiments. The full treatment of the problem is detailed and requires the calculation of the viscosity cross section and a collision integral [18, 19]. At low energies, helium-4 is unusual due to a combination of the nature of Bose-Einstein statistics with the low mass and inertness of the helium atoms. It can then be shown that properties of a free jet expansion strongly diverge from the expected classical behaviour [18, 19]. Some physical insight into how these quantum effects arise can be obtained by considering the low energy behaviour of the interatomic scattering of helium-4 atoms. The stability of a helium-4 atom leads to the only interatomic force being an extremely weak van der Waals interaction. It can be shown that for an attractive potential, the scattering cross section at low energy is inversely proportional to the bound state energy [20]. Helium-4 atoms can form a very weakly bound dimer due to the weak van der Waals force between the atoms [21], which leads to a large scattering cross section at low energies. Therefore, in a free jet expansion the collisions continue further out into the expansion, leading to an improved speed ratio.

Toennies and Winkelmann measured and simulated the speed ratio for helium-4 beams as a function of nozzle pressure [19]. Figure 3 shows an empirical fit to that model using the function,

$$\log(S) = a\log(P_0 d_{noz}) + b + \frac{c}{1 + e^{-\delta(\log(P_0 d_{noz}) - \mu)}}, \qquad (1)$$

where $a = 0.43 \pm 0.03$, $b = 0.76 \pm 0.02$, $c = 0.84 \pm 0.10$, $\delta = 5.2 \pm 0.9$ and $\mu = 1.97 \pm 0.03$ are fitted parameters to the model when $P_0 d_{noz}$ is measured in torr cm.

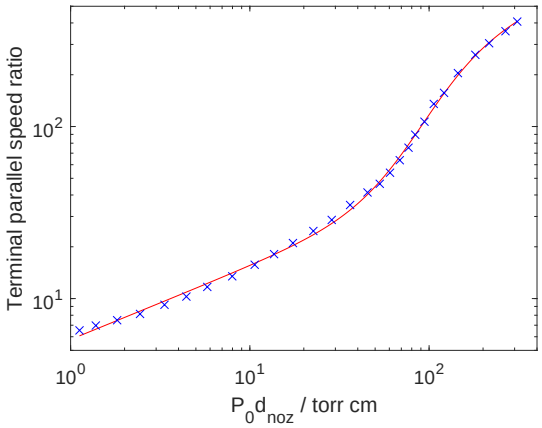

Figure 3: Empirical fit (red line) to the speed ratio model proposed by Toennies and Winkelmann [19] (blue crosses). The sharp increase in speed ratio at $P_0 d \approx 50$ torr cm is due to the onset of quantum cross-section effects. The fit given in equation 1 combines a straight line and logistic function to represent the classical and quantum contributions to the speed ratio.

The apparent spatial distribution of a free jet source can be described by introducing the concept of a virtual source [22]. At large enough distances from the source, collisions between helium atoms cease and the atoms follow straight line paths in a molecular flow regime. These trajectories can be traced back to an area of least confusion near the nozzle, with radius r_v, which we define as the virtual source. Collisions of the atoms near the nozzle usually lead to the virtual source being much larger than the nozzle aperture itself, and often larger than the skimmer. Virtual sources of free jet expansions have been shown to have a double Gaussian shape [23] which results in the virtual source having large tails around the central distribution. However the wide component of the source can be neglected if the source is suitably collimated after the expansion has terminated, i.e. only a small area from the centre of the expansion is used to form the final beam.

Following the treatment in Scoles [10], the point where the expansion terminates can be approximated by equating the terminal speed ratio to the point in the continuum expansion that has the corresponding Mach number. The result for a 10 µm

nozzle and 150 bar pressure, as typically used in [3, 4], was calculated by finding the terminal speed ratio using equation 1 and approximating the the continuum expansion using Table 2.2 in [10]. These conditions give the quitting surface as 3.3 mm from the nozzle, which is considerably less than the typically 10 mm distance between the nozzle and the skimmer, indicating that collimation of the virtual source should be possible. However, for instruments following the design outlined by Witham and Sánchez [24], with only 1 mm between the nozzle and the main aperture, it may not be possible to remove the wider component of the virtual source in this way.

2.2. Virtual Source Brightness

Most conventional atom-surface scattering experiments use wide beams to study a spatially homogeneous sample in reciprocal space. Since the beam is not spatially resolved, the size of the source is unimportant and only the intensity needs to be maximised. However for microscopy, we need a narrow and high intensity beam, so we instead need to maximise the brightness of the source.

We can define the brightness, B, of an atom beam source as

$$B = \frac{I}{\pi r_v^2}, \tag{2}$$

where I is the centerline intensity per steradian of the beam and r_v is the virtual source radius (as defined by DePonte et al. [25], which is $\sqrt{2}$ different from the usual definition of a Gaussian). To obtain a complete expression for the brightness we therefore require expressions for the centerline intensity and virtual source size.

DePonte et al. [25] show that the centerline beam intensity is proportional to the total flux through the nozzle. They obtain the constant of proportionality by fitting to experimental data. Their resulting expression is

$$I = 0.36 P_0 d_{noz}^2 (m k_B T_0)^{-\frac{1}{2}}, \tag{3}$$

where P_0 is the nozzle stagnation pressure in Pascals, d is the nozzle diameter in metres and T_0 is the stagnation temperature of the gas in Kelvin. There is deviation from the simple expression when the flux through the nozzle is high, which is attributed to skimmer interference effects [26]. These interference effects arise at high fluxes, when significant numbers of atoms are backscattered from the outer surface of the skimmer into the expansion, disturbing the trajectories of the expanding atoms.

The virtual source size is a more complex parameter to estimate, since quantum effects can influence the virtual source size and these are difficult to accurately model. However DePonte et al. [25] note that it is possible to obtain an approximate expression for the virtual source size in terms of the speed ratio. By using scaling arguments and fitting to experimental data, the authors obtain the approximate relationship[1],

$$r_v = 0.80 d_{noz} S^{0.52}, \tag{4}$$

[1]This expression differs from that given by DePonte et al. [25] due to a potential error in using the source diameter instead of the source radius.

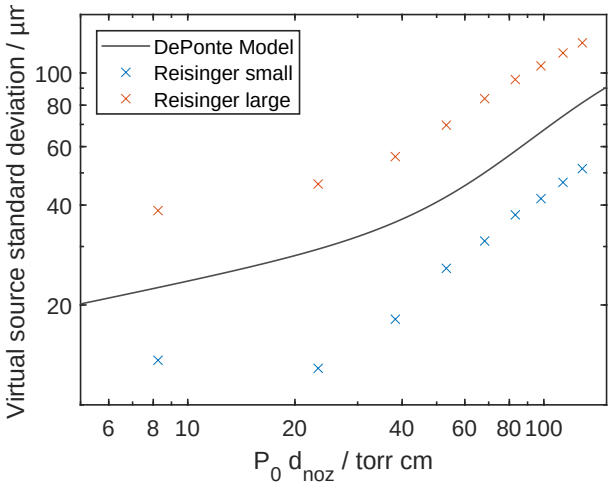

Figure 4: Comparison of the model from Deponte et al. for the virtual source size in equation 4 with experimental data for the large and small component of the expansion from a 10 µm nozzle, as measured by Reisinger et al. [23]. In order to compare the models, the source has been assumed to be Gaussian and the standard deviation has been plotted.

that captures the relative variation in source size with $P_0 d_{noz}$ and the absolute size to within a factor of order unity. Figure 4 shows a comparison of equation 4 with experimental data from Reisinger et al. [23] for a 10 µm nozzle at room temperature. The representative source size model from Deponte shows the same behaviour as the experimental data and an intermediate absolute size, thus providing some confidence in the form of the expression. Ideally a comprehensive body of new experimental source size data would be acquired and used here to refine the model, but obtaining such data is a significant undertaking and is beyond the scope of the present work.

We can combine equations 2, 3 and 4 to obtain an approximate expression for the brightness (count rate per steradian per unit area of the source) of a helium source,

$$B = 0.18 \frac{P_o}{S \sqrt{m k_B T}}. \tag{5}$$

Figure 5 shows the variation of brightness with nozzle pressure for 5 µm, 10 µm and 20 µm diameter nozzles, obtained by combining the brightness model in equation 5 with the empirical fit for the speed ratio plotted in Fig. 3. The quantum effects in the helium expansion that were discussed earlier cause the virtual source size to increase suddenly at between 30 and 100 bar (depending on nozzle size), so we see the brightness decreases at higher nozzle pressures. Extrapolation of the data for the speed ratio in fig. 3 leads to the brightness increasing again at even higher pressures. The brightness can therefore be maximised by either using a pressure just before the onset of quantum effects, or potentially by using a much higher nozzle pressure as shown in Fig. 5. However, the existence of the very high pressure maximum is speculative and additional experimental data needs to be collected to test the prediction. Even then, it would be difficult to practically realise a source that runs at these extremely high nozzle pressures; to use gas fixtures at greater than 1000 bar would pose significant technical challenges. We will

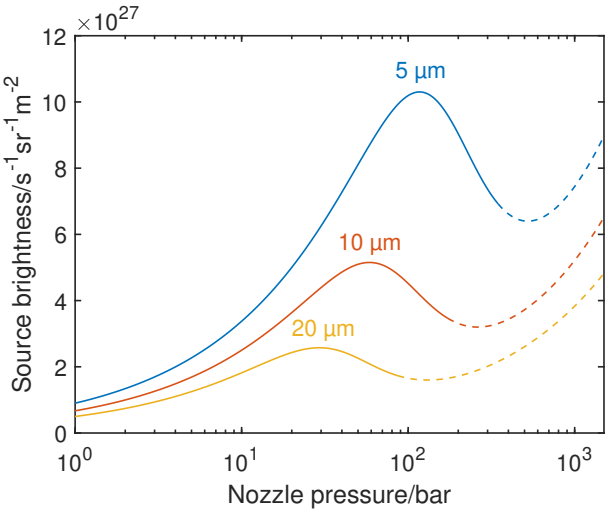

Figure 5: Brightness of a helium source modelled as a function of pressure for 5, 10 and 20 µm diameter nozzles. The sudden increase in the virtual source size causes the brightness to drop at about 50 bar for the 10 µm nozzle. The model used by Toennies and Winkelmann is only supported by experimental data up to $Pd \approx 100$ torr cm, so the extrapolation to higher pressures is indicated by a dashed line.

only consider an instrument operating near the lower pressure peak, which for a 10 µm nozzle is at about 60 bar, for the remainder of this work.

Experimental results from DePonte et al. [25] show the peak in brightness appearing at $P_0d \approx 10$ torr cm, which is lower than the expected value of $P_0d \approx 44$ torr cm from equation 5. The authors suggest that quantum effects on the perpendicular speed ratio become significant at lower values of P_0d than in the parallel speed ratio, which leads to larger than expected virtual source sizes. However, a more likely explanation for the discrepancy has been noted by Reisinger et al. [23] when the brightness peak was measured with a different setup at $P_0d \approx 20$ torr cm. The reduction in brightness begins at the same point when the intensity no longer follows the linear relationship given by equation 3. It was noted that it is likely that the observed reduction in intensity is due to backscattering from the skimmer [26] which can also explain the difference in the peak brightness condition that was observed by DePonte et al.

Given that it has already been shown that decreasing the nozzle diameter increases the brightness [25], it is reasonable to assume that future instruments will use smaller nozzles than are typically used in current atom scattering apparatus. Therefore, the total flux will be reduced and, since the centreline intensity is approximately given by $I \approx Q\exp(\eta Q)$ [27], where Q is the nozzle flow rate and η is a constant describing how much flux is backscattered, we would also expect that the reduction in intensity due to backscattering will be prevented. Given the experimental data that has been collected so far is likely to have been affected by backscattering effects, which future instruments are likely to eliminate, we will adopt the model proposed by DePonte et al. as presented in equation 5. By focussing on the fundamental brightness of a supersonic source, rather than the experimental results that include backscattering effects, we hope to obtain more accurate results – although we acknowledge that ignoring backscattering may lead to an overestimate of the achievable flux. New experimental work using small nozzles at high pressures with sufficient pumping would prove extremely useful in developing the model further, but is beyond the scope of the present work.

2.3. *Intensity and beam size in pinhole and zone plate geometries*

There are two established methods for creating a narrow beam of helium atoms: collimation with a small pinhole and focusing with a Fresnel zone plate. For the pinhole case, in addition to the geometric broadening shown in Fig. 1, the beam of atoms diffracts after the aperture, leading to additional broadening of the beam. The effect is a weak function of the speed ratio of the beam, so we can treat the pinhole as achromatic, meaning the helium beam production and collimation processes can be treated separately. In contrast, Fresnel zone plates [28] are strongly chromatic lenses [29] and focus with significant chromatic aberrations [17]. Equation 5 shows that the speed ratio is related to the brightness of the source, and therefore also the total flux in the beam. Since both the flux and size of the beam produced by zone plate focusing depend on the speed ratio they must be optimised together.

In order to compare these two focussing methods, we require a model for the intensity and size of the helium microprobe formed for both cases. In general, when the source size is similar in size to the skimmer being used, then the Sikora model is needed to obtain an accurate value for the centerline intensity [9]. An alternative derivation of the Sikora model using a virtual source is included in Appendix A. It is shown in the appendix that when a small point like skimmer is used, the Sikora model simplifies to the product of the brightness and the area of the skimmer. Since we have already established that it is advantageous to limit the source extent using a source aperture, as illustrated in Fig. 1, we will assume that the Gaussian shape of the source is not important and use equation A.12 so that the centreline intensity can be taken to be the product of the brightness and the area of the skimmer.

We first obtain an expression for the beam intensity at the optical element in the limit of skimmers that are smaller than the virtual source. Since brightness, B, is the number of atoms per steradian per unit area of the source, the flux of the helium beam per steradian can be obtained by multiplying by the area of the chosen source aperture, πx_s^2. Then since the angular size of the source, as seen from the optical element, is given by $\beta = x_s/r_s$, where r_s is the distance from the source to the aperture plane, the intensity (flux per unit area) at the optical element, I, is given by

$$I = \pi\beta^2 B. \tag{6}$$

Now that an expression for the intensity of the beam has been obtained, we derive expressions for the flux and beam standard deviation obtained using either a pinhole or a zone plate. To avoid any confusion over the definition of the term resolution, we describe the size of the helium microprobe with the term

beam standard deviation. The beam standard deviation, ϕ, is governed by three broadening effects for both the pinhole and the zone plate cases. In both cases, we assume that the effects can be approximated as Gaussian functions and be convoluted together such that the total beam width is given by $\phi_T^2 = \phi_1^2 + \phi_2^2 + \phi_3^2$. The general goal is therefore to approximate each of the broadening effects as a Gaussian function and obtain the standard deviation.

For a pinhole, the total transmitted flux is given by $F_\mathrm{p} = I\pi d^2/4$, where d is the diameter of the pinhole. We can then substitute with our expression for I in equation 6, which results in

$$F_\mathrm{p} = \frac{0.18\pi^2 P_o}{4\sqrt{mk_BT}}\frac{d^2\beta^2}{S}. \tag{7}$$

The beam standard deviation for the pinhole case, ϕ_p, is determined by the pinhole geometry, diffraction at the pinhole, and the finite source size. As previously stated, the total beam standard deviation can be estimated by convoluting the beam standard deviation obtained using geometric optics, the extent of the Airy disc diffraction pattern from the pinhole, and the (demagnified) size of the source.

The geometric pattern formed by the pinhole is a circle of diameter d, which we will approximate with a Gaussian distribution with a standard deviation given by $d/\left(2\sqrt{3}\right)$. The choice of standard deviation is difficult since we are trying to approximate a non-Gaussian function with a Gaussian function, but we have chosen to follow the approach used by Palau et al. [8] to maintain consistency. The distribution across the source aperture is uniform, which can similarly be approximated by a Gaussian with a standard deviation given by $\beta f/\sqrt{3}$, where f is the pinhole to sample working distance. The Airy function has its first zero at $1.22\lambda f/d$, but using this expression directly would overestimate the broadening. Instead, we approximate the central Airy disk with a Gaussian distribution [30] and use the subsequent standard deviation of $0.42\lambda f/d$. Combining these terms in quadrature gives the total beam standard deviation as

$$\phi_\mathrm{p} = \sqrt{\left(\frac{d}{2\sqrt{3}}\right)^2 + \left(\frac{\beta f}{\sqrt{3}}\right)^2 + \left(\frac{0.42\lambda f}{d}\right)^2}. \tag{8}$$

For a zone plate, the total flux in the beam is given by $F_\mathrm{zp} = \eta I\pi(r_N)^2$, where η is the efficiency of the zone plate and r_N is its radius. By substituting and using the continuum limit approximation $r_N = \lambda f/2\Delta r_N$, where Δr_N is the size of the outermost zone, we obtain the total flux in a zone plate focused beam,

$$F_\mathrm{zp} = \frac{0.18\pi^2 P_o}{4\sqrt{mk_BT}}\frac{\eta\beta^2\lambda^2 f^2}{S(\Delta r_N)^2}. \tag{9}$$

The theoretical efficiency of the first order focus of a zone plate is $\eta = 1/\pi^2 \approx 10\%$ [31]. The efficiency of a real zone plate has been experimentally measured by Reisinger et al. to be about 7% of the incident flux [32]. The remaining transmitted flux appears as a wide beam which contains a much higher flux than the first order focus. Eder et al. [33] have shown that the focus can be selected using a narrow aperture between the zone plate and the image plane known as a zero order stop.

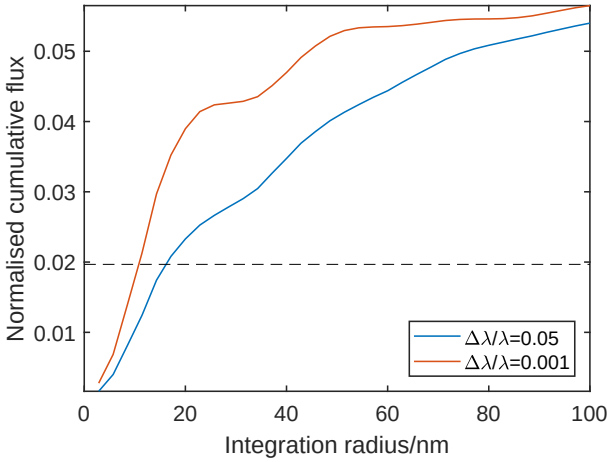

Figure 6: Simulation of the integrated flux from the centre of the focal spot produced by a zone plate with $f = 1\,\mathrm{mm}$, $\lambda = 5.63\times10^{-11}\,\mathrm{m}$, $\Delta r_N = 25\,\mathrm{nm}$ and 12 support bars that are 75 nm wide. For both speed ratios we see the flux leveling off, indicating the position of the edge of the central spot and showing that there is about 5% of the total flux in the central spot. The lower speed ratio produces a beam that has a larger distribution of flux due to the chromatic aberrations of the zone plate. The dashed line is the flux contained within one standard deviation of a Gaussian beam normalised to have a total flux of 5%, which is used to estimate the beam standard deviation.

A numerical simulation has been used to investigate the focal properties of a realistic zone plate for use with helium atoms. The wave equation can be solved using Green's functions and applying Rayleigh-Sommerfeld boundary conditions. The resulting equation can be expressed as a convolution and therefore can be solved using the convolution theorem and fast Fourier transforms. Diffracted intensity was calculated for a zone plate with $f = 1\,\mathrm{mm}$, $\Delta r_N = 25\,\mathrm{nm}$, $\lambda = 5.63\times10^{-11}\,\mathrm{m}$ (which corresponds to a nozzle temperature of $T = 300\,\mathrm{K}$) and the support structure illustrated in the inset in Fig. 1. Figure 6 shows the integrated flux in the central region (known as encircled energy in optics), including and around the central peak, for two different speed ratios. The results are normalised to the incident flux, and plotted cumulatively as a function of radius. The edge of the central peak is indicated by the cumulative flux leveling off as the integration radius is increased. The simulation shows that in both cases the central focus from the zone plate contains about 5% of the incident flux. The difference from the theoretical efficiency arises due to the conservative support structure design that deviates from the ideal zone plate design. We shall use $\eta = 0.05$ in subsequent calculations.

Compared to the pinhole case, predicting the size of the zone-plate focussed beam is harder, since the chromatic aberrations are difficult to predict accurately. In order to discuss the behavior, a representative example of a zone plate is needed, for which we use the parameters detailed in the previous paragraph. The simulated intensity profile across the spot is plotted in Fig. 7. The apparent full width half maximum of the central spot does not change significantly when the speed ratio is increased. However, there is a significant redistribution of the intensity, with more flux appearing in the central region and a reduction in the surrounding areas.

To progress with our optimisation, we need to represent these

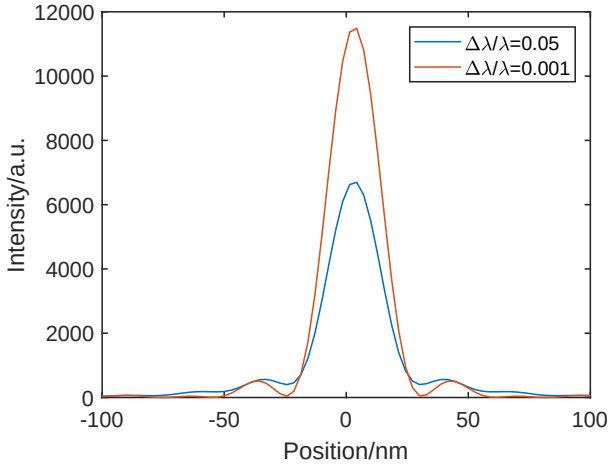

Figure 7: Section of the intensity in the spot produced at different speed ratios. The different speed ratios produce central spots with approximately the same full width half maximum. However, there the total flux in the central peak is lower for the lower speed ratio and more of the intensity appears outside where the first zero occurs for the monochromatic beam.

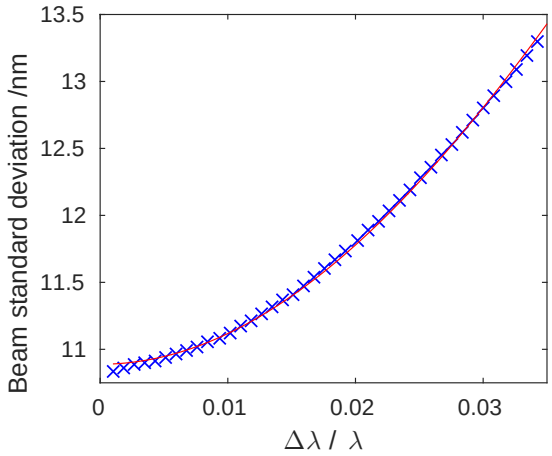

Figure 8: Beam size at different speed ratios for a zone plate with a focal length of 1 mm. The blue crosses are where the normalised integrated flux from the centre is equal to 0.020, which we are using an estimate for the beam standard deviation as discussed previously. The red line shows the model $\sigma_{\text{chrom}} = \sqrt{a^2 + (b(\Delta\lambda/\lambda))^2}$, with the parameters optimised using a least squares algorithm to be $a = (10.889 \pm 0.005)$nm and $b = (2.246 \pm 0.005) \times 10^{-7}$. Zone plate radius here is 1.14×10^{-6}, so gives correction factor as (5.066 ± 0.011).

differing distributions as a single representative standard deviation. One method is to use the integrated flux from the centre of the spot, as shown in Fig. 6, and estimate the standard deviation of the spot by comparison with an integrated 2D Gaussian function. Even though it is a substantial simplification, it should still be representative of the overall imaging resolution in a microscope since we are interested in the area of the sample that contains the helium flux. The integral of a normalised 2D Gaussian from the centre is $X(R) = 1 - \exp(-R^2/2\sigma^2)$, so when the radius of the integrated area is equal to the standard deviation we expect $1 - e^{-\frac{1}{2}}$ of the flux to be enclosed. The standard deviation of the beam size can therefore be estimated by finding when the integrated normalised flux is equal to $\left(1 - e^{-\frac{1}{2}}\right) \times 0.05 \approx 0.020$.

The variation of the estimated standard deviation of the beam with speed ratio is plotted in Fig. 8. The beam standard deviation is a convolution of the perfect diffraction pattern through a zone plate and the chromatic aberration which we wish to estimate. We fit a function of the form

$$\sigma_{\text{chrom}} = \sqrt{a^2 + \left(b\frac{\Delta\lambda}{\lambda}\right)^2}, \tag{10}$$

to the estimated beam size. The result is that $b = (2.246 \pm 0.005) \times 10^{-7}$. Previously the formula used has been $\sigma'_{\text{chrom}} = r_N \Delta\lambda/\lambda$ [7, 17], which predicts a chromatic aberration for a zone plate with a working distance of $f = 1$ mm and a minimum feature size of $\Delta r_N = 25$ nm of

$$\sigma'_{\text{chrom}} = 1.14 \times 10^{-6} \frac{\Delta\lambda}{\lambda}. \tag{11}$$

It should be noted that the size of the zone plate deviates significantly from the continuum result ($r_N = (\lambda f)/(2\Delta r_N)$) since there are so few zones. The result from our diffraction simulation gives a value that is (5.066 ± 0.011) times less than this expression, so we shall use a modified form of equation 11 for the chromatic aberration

$$\sigma_{\text{chrom}} = \frac{r_N}{5.066\sqrt{2}S}. \tag{12}$$

As before, the total beam standard deviation at the sample is found by combining the contributing broadening effects. These are the combination of the point spread function of the zone plate, the demagnified source size and the chromatic aberration.

The diffraction pattern obtained from a point source illuminating a zone plate is approximately an Airy pattern. The first zero from the diffraction pattern through the zone plate is at $1.22\Delta r_N$ [31], so using the same argument for Airy disks as the pinhole case, we approximate the diffraction pattern with a Gaussian that has a standard deviation given by $0.42\Delta r_N$.

The extended source is modelled in the same way as the pinhole case, as a uniform disk with an angular size of β. A demagnified image of the source is formed, which we approximate with a Gaussian that has a standard deviation of $\beta f/\sqrt{3}$.

Together, these give a beam that is approximated to be a Gaussian with a standard deviation given by,

$$\phi_{\text{zp}} = \sqrt{(0.42\Delta r_N)^2 + \left(\frac{\beta f}{\sqrt{3}}\right)^2 + \left(\frac{\lambda f}{10.13\sqrt{2}\Delta r_N S}\right)^2}. \tag{13}$$

3. Geometry Optimisation Method

In a helium microscope we generally wish to maximise both signal and resolution (i.e. maximise flux in the beam reaching the sample and minimise its size). However, these are incompatible quantities and there is no simultaneous optimum. Instead, given the helium flux at the sample is a function of many variables, we can develop an optimisation process to select a

microscope geometry that maximises flux for a particular (constrained) resolution.

As described above, given a set of parameters $\underline{x}$, we can find the flux $F(\underline{x})$ and the beam size $\phi(\underline{x})$ produced by a focusing element. We introduce a new function $g(\underline{x}) = \phi(\underline{x}) - \sigma$, which when set to $g(\underline{x}) = 0$, acts as the constraint, such that the beam standard deviation is our target standard deviation, σ. The constrained optimisation problem can be solved using Lagrange multipliers. We proceed by introducing the functional

$$\mathcal{L} = F(\underline{x}) - \Lambda g(\underline{x}), \tag{14}$$

and solutions are found by obtaining the maximal values of the Lagrange function, $\mathcal{L}$. We have opted to use Λ as the symbol for the Lagrange multiplier to avoid confusion with the wavelength. The maximum values are found by solving the system of equations defined by

$$\frac{\partial \mathcal{L}}{\partial \underline{x}} = 0, \tag{15}$$

where $\underline{x}$ represents any free variable in the system. Some of these variables do not have maxima and instead we must find their values from practical limitations. The set of equations produced may not be analytically solvable, in which case a numerical method will need to be used.

3.1. Analytic Solution for Pinhole Geometry

An analytic solution for the optimal flux in the beam from a pinhole can be obtained, since the source and atom optics are separable problems. Let the flux through the pinhole be given by

$$F_\mathrm{p} = \gamma d^2 \beta^2, \tag{16}$$

where γ is defined by $\gamma = \pi^2 B_\mathrm{peak}/4$ and B_peak is the optimised peak brightness from the source. We now need to optimise the Lagrange function,

$$\mathcal{L} = F - \Lambda(\phi - \sigma), \tag{17}$$

which gives

$$\mathcal{L} = \gamma d^2 \beta^2 - \Lambda \left(\sqrt{\left(\frac{d}{2\sqrt{3}}\right)^2 + \left(\frac{\beta f}{\sqrt{3}}\right)^2 + \left(\frac{a}{d}\right)^2} - \sigma \right), \tag{18}$$

where $a = 0.42\lambda f$ for simplicity.

We see that for the pinhole, the working distance, f, does not have an optimum value and should be minimised – although in reality is limited by fabrication capabilities. The remaining variables to be optimised are the Lagrange multiplier, Λ, the pinhole diameter, d, and the angular source size, β.

Differentiating equation 18 with respect to the Lagrange multiplier and setting it to zero gives

$$\frac{\partial \mathcal{L}}{\partial \Lambda} = (\phi - \sigma) = 0 \implies \phi = \sigma \tag{19}$$

Which specifies that the beam standard deviation must be given by our target resolution σ. Differentiating with respect to the angular source size gives

$$\frac{\partial \mathcal{L}}{\partial \beta} = 2\gamma d^2 \beta - \frac{\Lambda}{\sigma}\frac{\beta f^2}{3}, \tag{20}$$

and so given that, $\partial\mathcal{L}/\partial\beta = 0$,

$$\frac{\Lambda}{\sigma} = \frac{6\gamma d_o^2}{f^2}. \tag{21}$$

Similarly, differentiating with respect to the pinhole diameter gives

$$\frac{\partial \mathcal{L}}{\partial d} = 2\gamma\beta^2 d - \frac{\Lambda}{\sigma}\left(\frac{d}{12} - \frac{a^2}{d^3}\right), \tag{22}$$

and again, given that, $\partial\mathcal{L}/\partial d = 0$,

$$\frac{\Lambda}{\sigma} = \frac{2\gamma\beta_o^2 d_o^4}{\left(\frac{d_o^4}{12} - a^2\right)}. \tag{23}$$

Here, d_o and β_o are the optimum pinhole diameter and angular source size for our given target resolution σ. We can combine equations 21 and 23 to eliminate Λ and find an expression that relates the optimum angular source size to the optimum pinhole size

$$\frac{f^2\beta_o^2}{3} = \left(\frac{d_o^2}{12} - \frac{a^2}{d_o^2}\right) \tag{24}$$

Substituting back into our definition for σ (equation 19) gives the optimum pinhole diameter as

$$d_o = \sqrt{6}\sigma. \tag{25}$$

Similarly we can show that the optimum angular source size is given by

$$\beta_o = \frac{\sqrt{3}}{f}\left(\frac{\sigma^2}{2} - \frac{a^2}{6\sigma^2}\right)^{\frac{1}{2}}. \tag{26}$$

Using equations 21 and 23 we can show that the optimum flux, $F_o = \gamma\beta_o^2 d_o^2$, is given by

$$F_o = 3\gamma\left(\frac{3\sigma^4}{f^2} - (0.42\lambda)^2\right). \tag{27}$$

3.2. Zone Plate Geometry

We can apply a similar process to analyse the zone plate geometry. In general, the source properties affect the speed ratio, and hence the ultimate resolution through chromatic aberrations. However, these effects are only significant at very small beam standard deviations. At larger beam standard deviations it is possible to make an approximate separation of the source and zone-plate focussing, to obtain approximate analytic expressions for the optimum conditions. Appendix B contains an approximate analytic solution for large beam standard deviations.

However, for the narrow beams required for high resolution helium microscopy, chromatic aberrations are significant and equation B.5 is inadequate. A full expression for the flux can be obtained by combining equation 9 for the flux in the beam, with our empirically fitted function for the speed ratio, given in equation 1. It is not possible to analytically solve the resulting set of equations, so a numerical approach must be used. We have used the function `fmincon` in MATLAB to perform the numerical constrained optimisation. The function seeks to maximise

the flux in the beam, subject to the nonlinear constraint $g = 0$. Instead of directly using the flux and beam standard deviation, the functions are scaled appropriately such that the quantities are $O(1)$, so the numerical routine can converge more easily. The code to implement this optimisation is provided on GitHub and Zenodo[2].

The numerical approach was validated by comparing with the analytic solution determined for the pinhole geometry; the optimum brightness was substituted into equation 27 and used to obtain the optimum flux as a function of the target resolution. The fractional difference between the analytic expression and the fully numerical optimisation is always less than 2×10^{-9}.

4. Results and Discussion

4.1. Optimised configuration

We now present results obtained using the optimisation methods above, for a realistic configuration of a scanning helium microscope. To obtain results from the numerical optimisation, values for a specific geometry have been used as justified previously in the work including a working distance of f =1 mm and a zone-plate efficiency of $\eta = 0.05$. Unless otherwise specified, we use a helium-nozzle size of 10 µm.

The minimum feature size of the zone plate, Δr_N, is set by the practical limits of fabrication rather than any theoretical limit. Previous zone plates fabricated for microscopy had much larger radii and minimum feature sizes of about 50 nm [1]. Given our much smaller zone plates, and the steady progress in nanofabrication technology, we use $\Delta r_N = 25$ nm in the examples below.

The optimum angular source size for a zone plate and pinhole, as calculated by the numerical optimisation, are plotted in Fig. 9. The pinhole optimum angular size is the same as the one calculated analytically using equation 26. The optimum follows a straight line until diffraction effects become important and the optimum angular size drops much quicker. In Fig. 9, the optimum angular source size for a zone plate has a very small deviation from a straight line which occurs at small beam standard deviations due to the chromatic aberrations.

The optimum pinhole diameter has been plotted as a function of the target beam standard deviation in Fig. 10. The optimum pinhole diameter as calculated from the numerical optimisation fits our analytic expression of $d_o = \sqrt{6}\sigma$ to within a negligible error.

Figure 11 shows the variation of the optimum nozzle pressure with target resolution for the zone plate geometry, obtained by numerical optimisation. The horizontal dashed-line is the speed-ratio independent optimum, which applies to both the pinhole case and zone-plates producing a wide beam with a flux given by equation B.5. The speed-ratio independent optimum pressure corresponds to the peak in brightness on the 10 µm line shown in fig. 5. The solid-curve represents the full numerical solution for the zone plate geometry, and deviates from the approximate expression at small target beam standard deviations. Here, chromatic aberrations become increasingly important in

[2]M. Bergin, Zenodo, `https://doi.org/10.5281/zenodo.3364806`

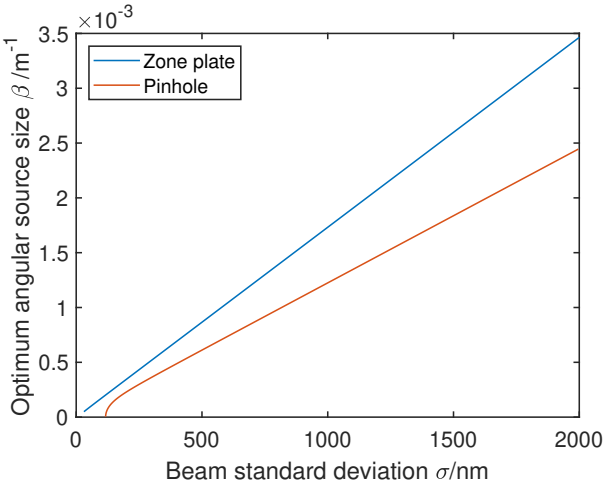

Figure 9: Plot of the optimum angular source as a function of beam standard deviation for both the pinhole and zone plate geometries. The pinhole optimum is approximately a straight line at larger beam standard deviations but then drops rapidly as the diffraction limit is reached. The zone plate optimum angular size also follows approximately follows a straight line with a small deviation at small beam standard deviations.

the zone plate focussing, broadening the focussed beam, and requiring a higher speed ratio beam. Achieving that speed ratio requires a higher nozzle pressure, even though the optimum pressure is no longer at the peak brightness.

The predicted optimum beam fluxes are plotted versus target beam standard deviation in Fig. 12, for both pinhole and zone plate geometries. The optimum flux for the pinhole setup approximately varies as $F_\mathrm{p} \propto \sigma^4$ (equation 27), while for the zone-plate setup approximately scales as $F_\mathrm{zp} \propto \sigma^2$ (equation B.5). Hence, the pinhole geometry is preferable at larger beam standard deviations, but as the target resolution is reduced the zone plate geometry becomes favourable. We can estimate the cross over point by equating equation 27 and equation B.5 and solving the resulting quadratic equation. We find that the cross over point is at

$$\sigma_\mathrm{co} = \frac{1}{\sqrt{3}}\sqrt{2\eta r_N^2 + \sqrt{\frac{4}{3}\eta^2 r_N^4 + (0.42\lambda f)^2(1-\eta)}}, \tag{28}$$

$$\sigma_\mathrm{co} \approx 2\sqrt{\frac{\eta}{3}}r_N, \tag{29}$$

which corresponds to a beam standard deviation of under 300 nm for the geometry considered. The assumptions made in section 2.3 mean that the absolute value of the beam flux may not be accurate, however we expect that the relative scaling between the zone plate and pinhole will be more accurate.

Appendix C contains representative tables of the key optimised properties for a series of target resolutions for the zone plate and pinhole geometries.

4.2. Achievable signal to noise

When acquiring images in a real microscope the contrast to noise ratio is a key metric for quantifying the image quality [34]. A related quantity is the signal to noise ratio which

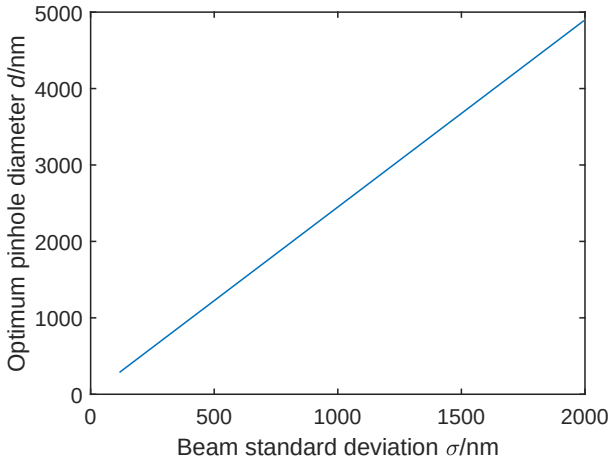

Figure 10: Plot of the numerically calculated optimum pinhole diameter as a function of the beam standard deviation for a pinhole geometry. The calculated optimum pinhole diameter follows the analytically expected function $d_o = \sqrt{6}\sigma$ to within 10^{-6} nm.

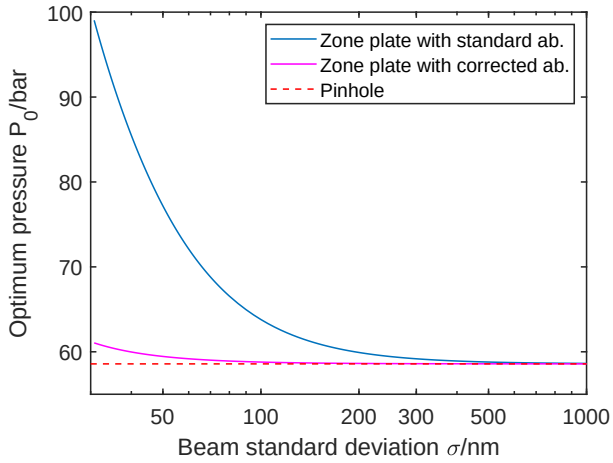

Figure 11: Plot of optimum nozzle pressure versus target beam standard deviation for the pinhole geometry (dashed-line) and zone-plate geometry (solid-curves) using the parameters given in the body text. The blue curve is obtained using a chromatic aberration modelled with $\sigma_{chrom} = r_N/(\sqrt{2}S)$, while the purple curve is obtained by using the corrected chromatic aberration term $\sigma'_{chrom} = r_N/(5.066\sqrt{2}S)$. The curves are obtained using the constrained numerical optimisation. At large target beam standard deviations zone-plate chromatic aberrations are insignificant and the optimum pressure corresponds to the brightness maximum in fig. 5. At smaller target standard deviations chromatic aberrations become significant and a higher speed ratio is needed, so the optimum pressure shifts from the brightness maximum.

contains similar information, except it does not account for the background or the actual contrast forming mechanism taking place at the sample, but focuses on the signal measured by the detector. SHeM images are usually limited by shot noise, so the signal to noise ratio can be used to determine the dwell time per pixel required to reduce the noise sufficiently to observe contrast. Images collected by Fahy et al. show that for a sample with large topographic changes and minimal background contributions, the images appear relatively noise free above a signal to noise ratio of about 30 [4]. Non-topographic contrast mechanisms will create smaller changes in the scattered helium distribution and so will require a better signal to noise ratio to observe.

Within a certain dwell time, Δt, the total signal per pixel is determined by the total (optimised) flux incident on the sample, F_{tot}, the proportion of atoms accepted by the detector, P_{acc}, and the efficiency of the detector, P_{det},

$$N_{\text{tot}} = F_{\text{tot}}\, P_{\text{acc}}\, P_{\text{det}}\, \Delta t. \tag{30}$$

We expect that the optimum conditions for maximising the signal to noise ratio will also maximise the image quality, but it should be noted that the experimental complications, including instabilities, background gases in the detector, and temperature variations throughout the system, are likely to significantly degrade the image quality (see figure 6.18(b) from Bergin [35] for further details). The probability of atoms scattering into the detector on the current machine in Cambridge can be estimated from the solid angle to be $P_{\text{acc}} \approx 0.5\%$, and a reasonable estimate for next generation detectors gives the detector efficiency as $P_{\text{det}} \approx 0.1\%$.

For a pinhole the signal to noise is given by $\sqrt{N_{\text{tot}}}$ since all the flux passing through the pinhole is in the beam. In the absence of any unwanted diffuse beams from insufficient differential pumping, the only helium incident on the surface is in the narrow beam formed by the pinhole.

For a zone-plate, only a small proportion of the total flux contributes to the central spot, while the majority of the signal forms a wide background. The zone plate has multiple focal points with a diminishing fraction of the flux outside of the first order focus, and a large component in the zero order of the beam that passes straight through the zone plate. The shot noise we expect is then given by $\eta N_{\text{tot}}/\sqrt{\alpha N_{\text{tot}}}$ where $\alpha = 0.374$ is the open fraction of the zone plate we are considering, and N_{tot} is the number of atoms that would be detected if the zone plate were replaced with a fully open aperture of the same radius. In deriving the expression we are assuming that the zero order beam is not contributing towards imaging and is simply acting as a background. Deconvolution of the diffraction pattern from the images could improve the signal to noise beyond the expression given above.

Figure 13 plots the signal to noise ratio expected for both pinhole and zone-plate geometries. For a zone plate without a zero order stop, the signal to noise ratio is reduced and the pinhole becomes the preferred method at lower beam sizes when compared to simply comparing the fluxes.

The performance of zone-plate focussing has been shown to be improved by introducing an aperture after the zone plate, to block the majority of the flux and only allow the central spot through[33]. In the case of a zero order stop, the expected signal to noise ratio is $\sqrt{\eta N_{\text{tot}}}$ since now the only flux of helium incident on the sample is in the main focussed beam.

The black-line in Fig. 13 shows the effect of the zero order stop, which increases the signal to noise ratio such that the cross over between the pinhole and zone plate geometry occurs in the same place as the flux comparison.

An approximate expression for the cross over point in the signal to noise ratio between a zone plate without a zero order stop and a pinhole can be derived in the same way as before.

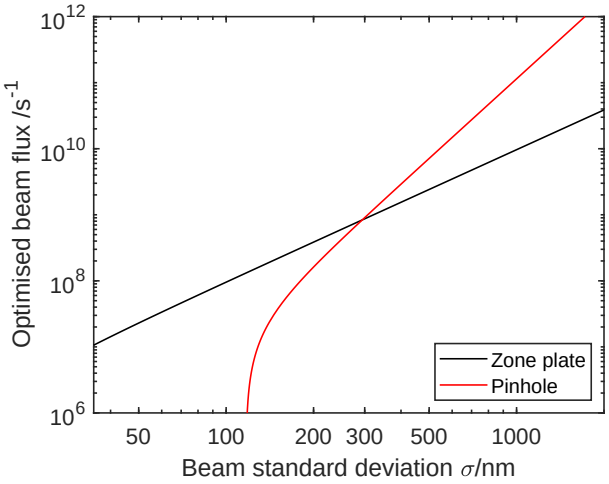

Figure 12: Plot of the optimum flux versus target beam standard deviation, obtained from a numerical constrained optimisation of the beam formed, in both zone-plate and pinhole geometries. At larger beam standard deviations the pinhole geometry delivers a greater optimum flux, but as the target standard deviation is reduced, the zone plate becomes the preferred method. The calculation was performed with the parameters described in the body text and a helium wavelength of $\lambda = 0.0563$ nm which corresponds to a room temperature beam.

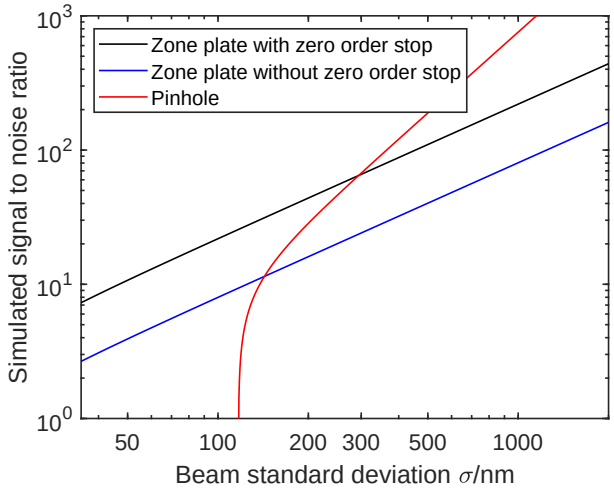

Figure 13: Plot of the optimum simulated signal to noise ratio for a dwell time of 1s as a function of target beam standard deviation for a pinhole and zone plate setup with and without a zero order stop. Without a zero order stop the signal to noise ratio is degraded and so the pinhole remains the preferred choice till smaller beam standard deviations. The calculation was performed with the parameters described in the body text and a helium wavelength of $\lambda = 0.0563$ nm. It should be noted that the effect of a background in the detector has been ignored, which is likely to influence the signal to noise at low fluxes.

Provided the source brightness is still at a maximum and therefore has not changed between the pinhole and zone plate cases (which may not be a good assumption if the chromatic aberrations are significant), the cross over point is given by

$$\sigma_{\mathrm{co},2} = \frac{1}{\sqrt{3}}\sqrt{2\frac{\eta^2}{\alpha}r_N^2 + \sqrt{\frac{4\eta^4}{3\alpha^2}r_N^4 + (0.42\lambda f)^2(1-\frac{\eta^2}{\alpha})}}, \quad (31)$$

$$\sigma_{\mathrm{co},2} \approx \frac{2\eta r_N}{\sqrt{3\alpha}}, \quad (32)$$

which corresponds to about 100 nm for the above optimisation. Since the chromatic aberrations are significant, the cross over prediction of the signal to noise ratio is not as accurate as the cross over of the flux predicted by equation 29.

4.3. Further improvements

So far, we have described a 'realistic optimum' configuration for a scanning helium microscope, including several parameters that were fixed by experimental constraints. It is useful to discuss these constraints further, and the potential for further improvement.

In the pinhole geometry, the working distance affects the optimised flux at the sample strongly, with one term varying as $F_{\mathrm{o,p}} \propto f^{-2}$ (equation 27). By lowering the working distance, larger angular source sizes can be used leading to higher fluxes through the pinhole. The microscope developed by Witham et al. [36] uses working distances typically between 10-50 µm and thus achieves very high fluxes. The trade off for very small working distances is that the depth of field will be reduced, and sample mounting and positioning becomes much more critical. Nonetheless, large gains can potentially be made from the 1mm reference working distance used here.

In the zone-plate geometry, the minimum feature size is a critical parameter, with one term varying as $F_{\mathrm{o,zp}} \propto \Delta r_n{}^{-2}$ (equation B.5). Reducing the minimum feature sizes leads to larger area zone plates that collect and focus a greater amount of helium. Larger zone plates lead to more severe chromatic aberrations, however for most resolutions this is not a limiting condition. Gains through the reduction of Δr_n will be limited by the development and advancement of nano-fabrication technologies.

The working distance in the zone plate geometry is a less important criteria, but should still be minimised. When the chromatic aberrations are negligible, the working distance is unimportant. As the working distance is increased, the decrease in the optimum source size is cancelled out by the increase in collection area. However, when chromatic aberrations are important, the optimum flux increases as the working distance decreases. The optimum flux depends asymptotically on the working distance, approaching a maximum value when the chromatic aberrations are negligible.

5. Summary and Conclusions

A method for optimising the geometry of a scanning helium microscope has been achieved by using a constrained optimisation of the flux arriving at a sample. For a pinhole arrangement the process can be performed analytically. In a zone-plate geometry, chromatic aberrations link the source properties with the zone-plate characteristics, so a numerical routine must be used to optimise the entire system. The method provides insight into both the optimised design and operating conditions of a microscope. We anticipate our method can be be applied to more complex models of both the beam intensity and beam

standard deviation, as new experimental data on these quantities becomes available.

Our optimisation process demonstrates that the beam flux drops very rapidly as the beam standard deviation is reduced; with the fourth and second powers of resolution for a pinhole and zone-plate respectively. To enable high-resolution measurements to be obtained within reasonable measurement times, future machines will require small working distances (relevant to pinholes) or fine feature sizes (relevant to zone-plates), combined with a high brightness source (small nozzle, high pressure) and extremely high efficiency detectors with negligible backgrounds as currently being developed [35, 37].

Acknowledgements

The work was supported by EPSRC grant EP/R008272/1. M.B. acknowledges an EPSRC studentship and a Leathersellers Graduate scholarship. The authors would like to thank Dr. W. Allison for several useful discussions.

Appendix A. Alternative derivation of Sikora model

The Sikora model was simultaneously derived by Anderson and Sikora in his PhD thesis [9] in 1973, and describes the on axis intensity from a free jet expansion that incorporates the physical size of the source and skimmer. The main feature of the model is that due to the source not being a point like object, the addition of a collimator (or skimmer as it is typically referred to now) will reduce the total intensity that would reach an on-axis detector. In the Sikora model, we consider the atoms to transition into molecular flow at the quitting surface, and the velocity distribution of the atoms can be determined from the speed ratio. Sikora then describes a series of complex approximations to solve the integrals and obtains an expression for the on axis intensity I as,

$$\left(\frac{I}{I_0}\right) \approx \left[1 - \exp\left(-S^2\left(\frac{r}{x_1}\right)^2\left(\frac{x_D}{x_D - x_C}\right)^2\right)\right], \tag{A.1}$$

where I_0 is the on axis intensity without any collimation, S is the speed ratio, r is the radius of the collimating aperture (skimmer), x_1 is the radius of the quitting surface, x_D is the distance from the nozzle to the detector and x_C is the distance from the nozzle to the collimator.

An equivalent expression can instead be derived by considering a virtual source model and calculating the on axis intensity after collimation. The brightness of the source, B, is defined as the on-axis intensity as measured from an infinitesimal part of the skimmer, so that $dI = B\,dA$ where dA is an infinitesimal area of the virtual source that is visible through the skimmer. The brightness in a supersonic expansion is usually described with a 2D Gaussian function,

$$B = Ke^{-\frac{\rho^2}{2\sigma^2}}, \tag{A.2}$$

where ρ is the radial distance from the centre of the nozzle, σ is the virtual source size as measured as the standard deviation of a Gaussian function and K is a normalisation factor for the function which is given by

$$K = \frac{I_0}{2\pi\sigma^2}. \tag{A.3}$$

Following the nomenclature used in Sikora's derivation, if a skimmer of radius r is used, then by considering similar triangles from the detector, the visible part of the virtual source has a size,

$$r_{\text{pro}} = \frac{x_D}{x_D - x_C} r. \tag{A.4}$$

The on-axis intensity can then be calculated by integrating the brightness,

$$I = \int B\,dA, \tag{A.5}$$

$$I = \int^{r_{\text{pro}}} Ke^{-\frac{\rho^2}{2\sigma^2}} \rho\,d\rho\,d\theta. \tag{A.6}$$

Performing a substitution of variables and computing the integral gives,

$$I = 2\pi K\sigma^2\left[1 - \exp\left(-\frac{r^2}{2\sigma^2}\left(\frac{x_D}{x_D - x_C}\right)^2\right)\right], \tag{A.7}$$

$$I = I_0\left[1 - \exp\left(-\frac{r^2}{2\sigma^2}\left(\frac{x_D}{x_D - x_C}\right)^2\right)\right]. \tag{A.8}$$

We can then relate equation A.8 back to a quitting surface model using the expressions derived by Beijerinck et al. [22]. The authors show in eq. (18), that for a quitting surface with a velocity component $v_\perp(z)$ perpendicular to the streamlines, characterised by $\alpha_\perp(z) = (2kT_\perp(z)/m)^{1/2}$, and assuming that all the molecules have the same parallel velocity $v_\parallel = u_\infty$ we find that the virtual source radius is given by,

$$R \equiv \sqrt{2}\sigma = \frac{z\,\alpha_\perp(z)}{u_\infty}. \tag{A.9}$$

Where z is the distance downstream from the nozzle. Beijerinck et al. also show in eq. (25) that the speed ratio is given by,

$$S = \frac{u_\infty}{\alpha(x_1)}. \tag{A.10}$$

However since the Sikora model only uses one temperature to model the behaviour at the quitting surface, we can then substitute into eq. A.9 and obtain,

$$R \equiv \sqrt{2}\sigma = \frac{x_1}{S}. \tag{A.11}$$

Therefore, the intensity expression derived in eq. A.8 is equivalent to the Sikora model in eq. A.1.

Additionally, the full expression for a finite size aperture is relatively complex and the exponential term means that it is difficult to obtain analytic expressions for the optimum conditions. Instead, consider the limit of a small skimmer and $x_D >> x_C$, so that after Taylor expanding the exponential function the intensity is approximately given by,

$$I \approx I_0\,\frac{r^2}{2\sigma^2}, \tag{A.12}$$

which after some rearrangement with a factor of π gives the product of the normalisation constant K of the brightness and the size of the skimmer. Therefore it is possible to vastly reduce the complexity of the Sikora model in the limit of small skimmers since the brightness is approximately constant in the centre of the expansion provided that,

$$r \ll \sqrt{2}\sigma\left(1 - \frac{x_C}{x_D}\right). \tag{A.13}$$

Appendix B. Approximate analytic solution for a zone plate

Let the flux through the zone-plate be given by

$$F = \gamma\beta^2\eta(2r_N)^2, \tag{B.1}$$

where γ is defined as before. In terms of the minimum feature size, Δr_N, we obtain

$$F = \frac{\gamma\eta\lambda^2 f^2}{{\Delta r_N}^2}\beta^2. \tag{B.2}$$

Since chromatic aberrations are negligible at large beam standard deviations, we can make the reasonably crude assumption that,

$$\left(\frac{\lambda f}{10.13\sqrt{2}\Delta r_N S}\right)^2 \ll (0.42\Delta r_N)^2 + \left(\frac{\beta f}{\sqrt{3}}\right)^2. \tag{B.3}$$

So then equation 13 for the total beam standard deviation can be simplified to,

$$\phi_{zp} = \sqrt{(0.42\Delta r_N)^2 + \left(\frac{\beta f}{\sqrt{3}}\right)^2}, \tag{B.4}$$

Since the speed ratio has been eliminated, we can directly substitute into the expression for the flux. Similarly to before, we can impose that the beam standard deviation, ϕ_{zp}, must be equal to a target resolution, σ, such that $\phi_{zp} = \sigma$. The only remaining free variables are β and f which appear as a pair and can be substituted for. Hence, the expression for the flux in the zone-plate focused beam, in the absence of chromatic aberrations, is

$$F_o = 3\gamma\eta\lambda^2\left(\frac{\sigma^2}{{\Delta r_N}^2} - (0.42)^2\right). \tag{B.5}$$

Appendix C. Optimised example geometries

Tables C.1 and C.2 provide a series of optimised example geometries for both zone-plate and pinhole configurations with target resolutions of 750, 500, 250, 100, 50 and 30 nm.

σ/nm	$F/10^7\mathrm{s}^{-1}$	x_s/μm	P_0/bar
750	544	260	58.6
500	242	173	58.6
250	60.3	86.5	58.6
100	9.55	34.4	58.8
50	2.3	16.9	59.5
30	0.749	9.64	61.2

Table C.1: Optimum properties of a zone plate geometry with a nozzle diameter of d_{noz} = 10 μm, a distance from the source aperture to the zone plate of r_s =100 mm, a working distance of f = 1 mm, a zone-plate efficiency of η = 0.05 and a minimum feature size of the zone plate of Δr_N = 25 nm. σ is the target beam standard deviation, F is the optimum flux, β is the optimum angular source size and P is the optimum source pressure.

σ/nm	$F/10^7\mathrm{s}^{-1}$	x_s/μm	P_0/bar	d/μm
750	3620	184	58.6	1.84
500	713	122	58.6	1.22
250	42.6	59.8	58.6	0.612
100	-	-	-	-
50	-	-	-	-
30	-	-	-	-

Table C.2: Optimum properties of a pinhole geometry with a nozzle diameter of d_{noz} = 10 μm, a distance from the source aperture to the zone plate of r_s =100 mm and a working distance of f = 1 mm. σ is the target beam standard deviation, F is the optimum flux, β is the optimum angular source size, P is the optimum source pressure and d is the pinhole diameter. The diffraction limit is reached at $\sigma_{\mathrm{lim}} = \sqrt{0.42\lambda f}/3^{1/4}$, so the smallest beam standard deviations cannot be achieved with a pinhole.

References

[1] M. Koch, S. Rehbein, G. Schmahl, T. Reisinger, G. Bracco, W. E. Ernst, B. Holst, Imaging with neutral atoms—a new matter-wave microscope, Journal of Microscopy 229 (1) (2008) 1–5. doi:10.1111/j.1365-2818.2007.01874.x.
URL http://onlinelibrary.wiley.com/doi/10.1111/j.1365-2818.2007.01874.x/abstract

[2] P. Witham, E. Sanchez, Simplified neutral atom microscopy, in: 2011 11th IEEE Conference on Nanotechnology (IEEE-NANO), 2011, pp. 535–540. doi:10.1109/NANO.2011.6144498.

[3] M. Barr, A. Fahy, A. Jardine, J. Ellis, D. Ward, D. A. MacLaren, W. Allison, P. C. Dastoor, A design for a pinhole scanning helium microscope, Nuclear Instruments and Methods in Physics Research Section B: Beam Interactions with Materials and Atoms 340 (2014) 76–80. doi:10.1016/j.nimb.2014.06.028.
URL http://www.sciencedirect.com/science/article/pii/S0168583X1400648X

[4] A. Fahy, M. Barr, J. Martens, P. C. Dastoor, A highly contrasting scanning helium microscope, Review of Scientific Instruments 86 (2) (2015) 023704. doi:10.1063/1.4907539.
URL http://scitation.aip.org/content/aip/journal/rsi/86/2/10.1063/1.4907539

[5] D. B. Williams, C. B. Carter, Transmission electron microscopy: a textbook for materials science / David B. Williams and C. Barry Carter., Plenum, New York, New York ; London, 1996.

[6] A. M. Donald, The use of environmental scanning electron microscopy for imaging wet and insulating materials, Nature Materials 2 (8) (2003) 511–516. doi:10.1038/nmat898.
URL https://www.nature.com/articles/nmat898

[7] A. Salvador Palau, G. Bracco, B. Holst, Theoretical model of the helium zone plate microscope, Physical Review A 95 (1) (2017) 013611. doi:10.1103/PhysRevA.95.013611.
URL https://link.aps.org/doi/10.1103/PhysRevA.95.013611

[8] A. S. Palau, G. Bracco, B. Holst, Theoretical model of the helium pinhole microscope, Physical Review A 94 (6) (2016) 063624. doi:10.1103/PhysRevA.94.063624.
URL https://link.aps.org/doi/10.1103/PhysRevA.94.063624

[9] G. S. Sikora, Analysis of asymptotic behavior of free jets: prediction of molecular beam intensity and velocity distributions. (1973).

[10] G. Scoles, D. Bassi, U. Buck, D. C. Laine (Eds.), Atomic and Molecular Beam Methods: Volume 1, Oxford University Press, New York, 1988.

[11] K. F. Riley, M. P. Hobson, S. J. Bence, Mathematical Methods for Physics and Engineering: A Comprehensive Guide, 3rd Edition, Cambridge University Press, Cambridge ; New York, 2006.

[12] G. Stephenson, Mathematical methods for science students. (2nd ed)., Longmans Scientific & Technical, Harlow, London, 1973.

[13] T. Kaltenbacher, Optimization of a constrained linear monochromator design for neutral atom beams, Ultramicroscopy 163 (2016) 62–68. doi:10.1016/j.ultramic.2016.02.003.
URL http://www.sciencedirect.com/science/article/pii/S0304399116300109

[14] M. Barr, K. M. O'Donnell, A. Fahy, W. Allison, P. C. Dastoor, A desktop supersonic free-jet beam source for a scanning helium microscope (SHeM), Measurement Science and Technology 23 (10) (2012) 105901. doi:10.1088/0957-0233/23/10/105901.
URL http://iopscience.iop.org/0957-0233/23/10/105901

[15] J. Braun, P. K. Day, J. P. Toennies, G. Witte, E. Neher, Micrometer-sized nozzles and skimmers for the production of supersonic He atom beams, Review of Scientific Instruments 68 (8) (1997) 3001–3009. doi:10.1063/1.1148233.
URL http://aip.scitation.org/doi/abs/10.1063/1.1148233

[16] R. Flatabø, S. D. Eder, A. K. Ravn, B. Samelin, M. M. Greve, T. Reisinger, B. Holst, Fast resolution change in neutral helium atom microscopy, Review of Scientific Instruments 89 (5) (2018) 053702. doi:10.1063/1.5029385.
URL https://aip.scitation.org/doi/10.1063/1.5029385

[17] S. D. Eder, T. Reisinger, M. M. Greve, G. Bracco, B. Holst, Focusing of a neutral helium beam below one micron, New Journal of Physics 14 (7) (2012) 073014. doi:10.1088/1367-2630/14/7/073014.
URL http://iopscience.iop.org/1367-2630/14/7/073014

[18] J. O. Hirschfelder, Molecular theory of gases and liquids., Structure of matter series, Wiley, New York, 1954.

[19] J. P. Toennies, K. Winkelmann, Theoretical studies of highly expanded free jets: Influence of quantum effects and a realistic intermolecular potential, The Journal of Chemical Physics 66 (9) (1977) 3965–3979. doi:10.1063/1.434448.
URL http://aip.scitation.org/doi/10.1063/1.434448

[20] J. J. Sakurai (Jun John) author, Modern quantum mechanics / J.J. Sakurai (late, University of California, Los Angeles) ; San Fu Tuan, editor (University of Hawaii, Manoa)., revised edition. Edition, Addison-Wesley, Reading, Mass. ; Wokingham, Reading, MA, 1994.

[21] J. P. Toennies, Helium clusters and droplets: microscopic superfluidity and other quantum effects†, Molecular Physics 111 (12-13) (2013) 1879–1891. doi:10.1080/00268976.2013.802039.
URL https://doi.org/10.1080/00268976.2013.802039

[22] H. C. W. Beijerinck, N. F. Verster, Absolute intensities and perpendicular temperatures of supersonic beams of polyatomic gases, Physica B+C 111 (2–3) (1981) 327–352. doi:10.1016/0378-4363(81)90112-1.
URL http://www.sciencedirect.com/science/article/pii/0378436381901121

[23] T. Reisinger, G. Bracco, S. Rehbein, G. Schmahl, W. E. Ernst, B. Holst, Direct Images of the Virtual Source in a Supersonic Expansion, The Journal of Physical Chemistry A 111 (49) (2007) 12620–12628. doi:10.1021/jp076102u.
URL http://dx.doi.org/10.1021/jp076102u

[24] P. Witham, E. Sánchez, A simple approach to neutral atom microscopy, Review of Scientific Instruments 82 (10) (2011) 103705. doi:10.1063/1.3650719.
URL http://scitation.aip.org/content/aip/journal/rsi/82/10/10.1063/1.3650719

[25] D. P. DePonte, S. D. Kevan, F. S. Patton, Brightness of micronozzle helium source, Review of Scientific Instruments 77 (5) (2006) 055107. doi:10.1063/1.2198813.
URL http://aip.scitation.org/doi/abs/10.1063/1.2198813

[26] H. Hedgeland, A. P. Jardine, W. Allison, J. Ellis, Anomalous attenuation at low temperatures in high-intensity helium beam sources, Review of Scientific Instruments 76 (12) (2005) 123111. doi:10.1063/1.2149008.
URL http://aip.scitation.org/doi/abs/10.1063/1.2149008

[27] M. J. Verheijen, H. C. W. Beijerinck, W. A. Renes, N. F. Verster, A quantitative description of skimmer interaction in supersonic secondary beams: Calibration of absolute intensities, Chemical Physics 85 (1) (1984) 63–71. doi:10.1016/S0301-0104(84)85173-3.
URL http://www.sciencedirect.com/science/article/pii/S0301010484851733

[28] O. Carnal, M. Sigel, T. Sleator, H. Takuma, J. Mlynek, Imaging and focusing of atoms by a fresnel zone plate, Physical Review Letters 67 (23) (1991) 3231–3234. doi:10.1103/PhysRevLett.67.3231.
URL http://link.aps.org/doi/10.1103/PhysRevLett.67.3231

[29] E. Hecht, Optics, 4th Edition, Addison-Wesley, Reading, Mass, 2001.

[30] B. Zhang, J. Zerubia, J.-C. Olivo-Marin, Gaussian approximations of fluorescence microscope point-spread function models, Applied Optics 46 (10) (2007) 1819–1829. doi:10.1364/AO.46.001819.
URL https://www.osapublishing.org/abstract.cfm?uri=ao-46-10-1819

[31] D. Attwood, Soft X-Rays and Extreme Ultraviolet Radiation: Principles and Applications, 1st Edition, Cambridge University Press, Cambridge, 2007.

[32] T. Reisinger, S. Eder, M. M. Greve, H. I. Smith, B. Holst, Free-standing silicon-nitride zoneplates for neutral-helium microscopy, Microelectronic Engineering 87 (5–8) (2010) 1011–1014. doi:10.1016/j.mee.2009.11.107.
URL http://www.sciencedirect.com/science/article/pii/S0167931709007710

[33] S. D. Eder, A. K. Ravn, B. Samelin, G. Bracco, A. S. Palau, T. Reisinger, E. B. Knudsen, K. Lefmann, B. Holst, Zero-order filter for diffractive focusing of de Broglie matter waves, Physical Review A 95 (2) (2017) 023618. doi:10.1103/PhysRevA.95.023618.
URL https://link.aps.org/doi/10.1103/PhysRevA.95.023618

[34] F. Timischl, The contrast-to-noise ratio for image quality evaluation in scanning electron microscopy, Scanning 37 (1) (2015) 54–62. doi:10.1002/sca.21179.
URL https://onlinelibrary.wiley.com/doi/abs/10.1002/sca.21179

[35] M. Bergin, Instrumentation and contrast mechanisms in scanning helium microscopy, Thesis, University of Cambridge (Apr. 2019). doi:10.17863/CAM.37853.
URL https://www.repository.cam.ac.uk/handle/1810/290645

[36] P. Witham, E. Sánchez, Exploring neutral atom microscopy, Crystal Research and Technology 49 (9) (2014) 690–698. doi:10.1002/crat.201300401.
URL http://onlinelibrary.wiley.com/doi/10.1002/crat.201300401/abstract

[37] A. R. Alderwick, A. P. Jardine, H. Hedgeland, D. A. MacLaren, W. Allison, J. Ellis, Simulation and analysis of solenoidal ion sources, Review of Scientific Instruments 79 (12) (2008) 123301. doi:10.1063/1.3030858.
URL https://aip.scitation.org/doi/10.1063/1.3030858